Article

Numerical Analysis of High-Velocity Oxygen Fuel Thermal-Spray Process for Fe-Based Amorphous Coatings

Jianxing Yu [1,2], Xin Liu [1,2,*], Yang Yu [1,2], Haoda Li [1,2], Pengfei Liu [1,2], Ruoke Sun [1,2], Limin Wang [3] and Pengfei Li [4,*]

[1] State Key Laboratory of Hydraulic Engineering Simulation and Safety, Tianjin University, Tianjin 300072, China; yjx2000@tju.edu.cn (J.Y.); yangyu@tju.edu.cn (Y.Y.); lihaoda@tju.edu.cn (H.L.); m13920367969@163.com (P.L.); srk_@tju.edu.cn (R.S.)
[2] Tianjin Key Laboratory of Port and Ocean Engineering, Tianjin University, Tianjin 300072, China
[3] State Key Laboratory of Metastable Materials Science and Technology, School of Materials Science and Engineering, YanShan University Qinhuangdao, Qinhuangdao 066004, China; LiminWang@ysu.edu.cn
[4] School of Resources and Materials, Northeastern University at Qinhuangdao, Qinhuangdao 066004, China
* Correspondence: lx_2020@tju.edu.cn (X.L.); lipengfei@neuq.edu.cn (P.L.)

Abstract: High-velocity oxygen fuel (HVOF)-sprayed amorphous alloy coatings usually have advantages of a dense structure that improve their resistance to corrosion, wear, and fatigue in the substrate. The flame flow characteristics and particle behaviors during the spray process have a significant influence on the amorphous coating structure and properties. In this study, a computational fluid dynamics model is enforced to analyze the flame flow and Fe-based amorphous alloy particle behavior in an HVOF spray process. The flame flow temperature, velocity characteristics, and the $Fe_{48}Cr_{15}Mo_{14}C_{15}B_6Y_2$ Fe-based amorphous alloy particles' velocities, temperatures, flight trajectories, and mass concentration distribution characteristics are simulated. Moreover, the effects of the oxygen/fuel ratio, particle morphology parameter, particle-injection rate, and angle on the particle behavior are also investigated. Judging from the simulation results, the optimum amorphous alloy particle size varies between 20 and 30 μm, the shape factor is within the range of 0.9–1, the optimum O/F ratio is 3.4, the optimum injection angle is 45°, and the optimum injection rate is 10 m/s. With these conditions, most of the particles settled toward the centerline of the spray gun and are in a semisolid or solid state before affecting the substrate, giving the materials optimal coating structure and performance.

Keywords: HVOF; Fe-based amorphous coating; flame flow characteristics; particle dynamics

Publisher's Note: MDPI stays neutral with regard to jurisdictional claims in published maps and institutional affiliations.

Copyright: © 2021 by the authors. Licensee MDPI, Basel, Switzerland. This article is an open access article distributed under the terms and conditions of the Creative Commons Attribution (CC BY) license (https://creativecommons.org/licenses/by/4.0/).

1. Introduction

Corrosion and wear of as well as fractures on materials' surfaces and interfaces are major issues in engineering environments, which not only lead to significant economic losses but also to enormous personal harm caused by these material failures. In China alone, the cost of corrosion of materials within engineering components amounts to billions of dollars or approximately 3.34% of the country's Gross Domestic Product (GDP) according to Hou et al.'s statistics [1]. Many researchers have studied surface engineering to explore superior coatings deposited onto metallic materials to overcome deterioration, among which amorphous alloys exhibit the excellent advantages of corrosion resistance, superior wear resistance, high mechanical strength, and high hardness, ensuing from their special disordered atomic structure [2–5]. In the past decade, a large number of bulk metallic glasses with a high glass-forming ability (GFA) have been developed in Pd-, Mg-, Zr-, and Fe-based systems using various rapid solidifying techniques [6–9]. Nevertheless, these bulk metallic glasses typically exhibit no work hardening or plastic deformation during room temperature deformation that considerably limits their applications as structural materials. To avoid this situation and simultaneously give play to their unique anticorrosion and wear-resistant properties, these materials are made into coatings.

Thermal spray technologies provide sufficient rapid cooling rates that inhibit long-range diffusion and avoid crystallization, existing as an alternate approach to beat scale disadvantages and increase the industrial applications of amorphous alloys. Many studies have attempted to manufacture Fe-based amorphous alloy coatings using various spraying methods, e.g., high-velocity oxygen fuel (HVOF) spraying [10,11], plasma spraying [12,13], laser cladding [14], and kinetic spraying [15]. Among these methods, HVOF spraying has attracted additional attention because of its benefits of low temperature and high velocity, which are conducive to manufacturing dense or low-porosity amorphous alloy coatings [16]. The complexity of HVOF thermal spraying in terms of its complex physics and multiscale interactions of variables makes it difficult to determine production parameters directly [17]. In the past decade, many amorphous alloy coatings have been prepared experimentally. Many experimental procedures in previous studies aimed to correlate the manufacturing parameters against coatings microstructure and properties [18,19]. However, to obtain high-quality Fe-based amorphous alloy coatings with homogeneous structure and high amorphous content, several trial-and-error attempts are needed, which consumes plenty of time and leads to high experimental costs. Simultaneously, it is troublesome to reveal the transient rule of gas and the particle flight history in HVOF spraying through experimental methods. Therefore, in addition to intuitive experimental exploration, it is necessary to gain a deeper understanding of the spraying mechanism [20]. Some simulations of the HVOF spraying process have been carried out [21–24]; however, these were mainly focused on WC–12Co and Ni–Cr materials, whereas, to our knowledge, studies on amorphous alloy coatings are relatively lacking. However, the excellent performance of amorphous coatings cannot be ignored by researchers, and a variety of amorphous alloy coatings have been applied in industry. Therefore, through computer simulations of HVOF spraying, the momentum and heat transfer between the flame flow and amorphous alloy particles can be analyzed in detail, which provides theoretical guidance for improving the properties of Fe-based amorphous coatings [25,26].

In the HVOF spraying process, the coating performance mainly depends on the behavior of particles close to the substrate surface [21,27,28], which is affected by the physical and chemical state at the moment of particle impact. With the increase in the impact velocity, the degree of flattening of the amorphous alloy particles increases, and the contact area between the particles and the substrate becomes larger, which improves the bonding strength and compactness of the coating and forms a high-performance coating. During the spraying process, the high temperature will cause the molten amorphous alloy particles to stick to the inner wall of the gun barrel, affecting the normal spraying process. In addition, the high temperature can also lead to partial oxidation of the amorphous alloy powder and increase the porosity of the coating. When the particles are in a molten or semimolten state, they form denser coatings with better corrosion resistance. Obviously, the particle velocity, particle temperature, and melting state have significant influence on the coating performance [17]. Therefore, the temperature, trajectory, and velocity of those amorphous alloy particles should be controlled to manufacture repeatable coatings.

To better analyze the HVOF spraying process and manufacture the corrosion- and wear-resistant Fe-based amorphous alloy coatings, the $Fe_{48}Cr_{15}Mo_{14}C_{15}B_6Y_2$ (SAM1651) amorphous alloy is chosen as the spray material owing to its excellent corrosion resistance and glass forming ability (GFA). The alloy features a nominal critical cooling rate of 80 K/s, suggesting that it can be cooled to an entirely glass state. In this study, the JP-5220 spray gun (Praxair, Danbury, CT, USA) is the object of analysis, and the gas flow and particle motion models for HVOF spraying are established based on computational fluid dynamics (CFD). The transient rules of the composition changes, flame characteristics, and particle distribution in the HVOF spray process are analyzed.

2. Models and Methods

Figure 1 shows a model diagram of the HVOF thermal spraying, including the kerosene and oxygen inlet, the combustion chamber, the Laval spray nozzle, and the

spray barrel. Figure 1a shows the two-dimensional (2D) model of the spray gun, and the detailed model parameters are annotated in figure and shown in Table 1. In this study, the three-dimensional (3D) calculation model shown in Figure 1b is used; that is, the 2D model is rotated 360°.
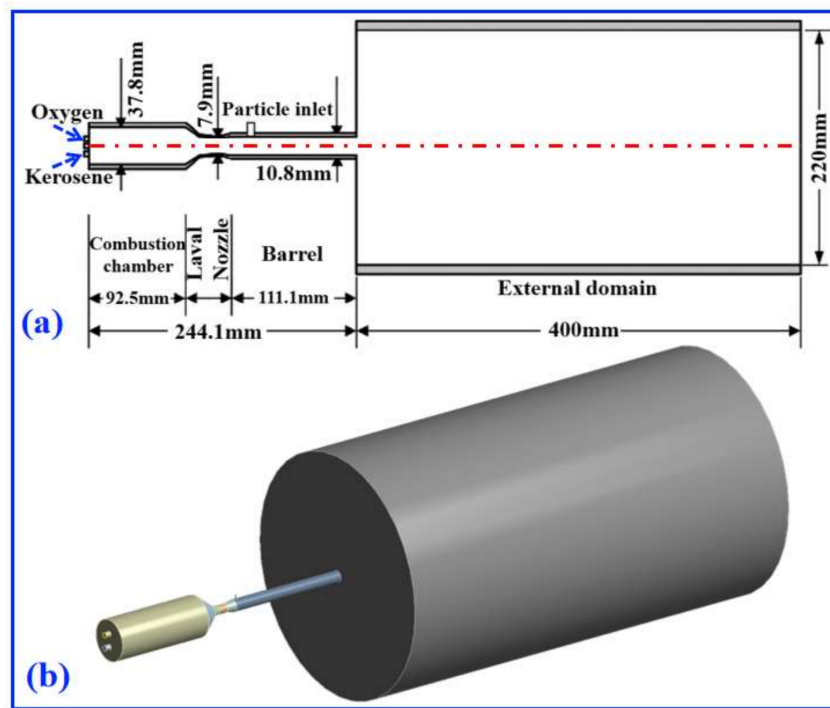

Figure 1. High-velocity oxygen fuel (HVOF) spray gun (**a**) two-dimensional (2D) model, and (**b**) three-dimensional (3D) model.

Table 1. High-velocity oxygen fuel (HVOF) spray model parameter.

Model Parameter	Values
The length of combustion chamber	92.5 mm
The width of the combustion chamber	37.8 mm
The length of the spray barrel	111.1 mm
The width of the spray barrel	10.8 mm
The length of external field cylindrical domain	400 mm
The width of external field cylindrical domain	220 mm

Figure 2a shows the computational mesh of the spraying model. The ICEM software (Fluent 19.0) is used to mesh the calculation domain. There are 1,282,729 elements and 1,243,608 nodes in the entire domain, and the elements sizes are in the range of 0.2–2 mm. The mean quality of elements is 0.897. To ensure the accuracy of the calculation, a hexahedral element is selected for depicting the combustion chamber and external region, as shown in Figure 2b,d, and a tetrahedral element is used for depicting the barrel part, as shown in Figure 2c. In addition, the external region is divided into two parts and uses a transitional grid, whereas the internal grid is refined. The refinement of the external region is conducive to accurately obtaining the flame flow characteristics and particle trajectories. Oxygen and kerosene are injected into the spray gun at flow rates of 0.02163 and 0.007 kg/s, respectively. Table 2 presents the property parameters of the SAM1651 amorphous alloy, where the material's density is 7310 kg/m^3 and the C_p is 460 J/(kg K). By adjusting the nitrogen gas flow, the particle injection rate varies from 5 to 20 m/s. It is assumed that the wall temperature of the HVOF spray gun is 300 K. The pressure far field and pressure outlet boundary are applied at the external domain, and the atmospheric pressure is 1.01 KPa.
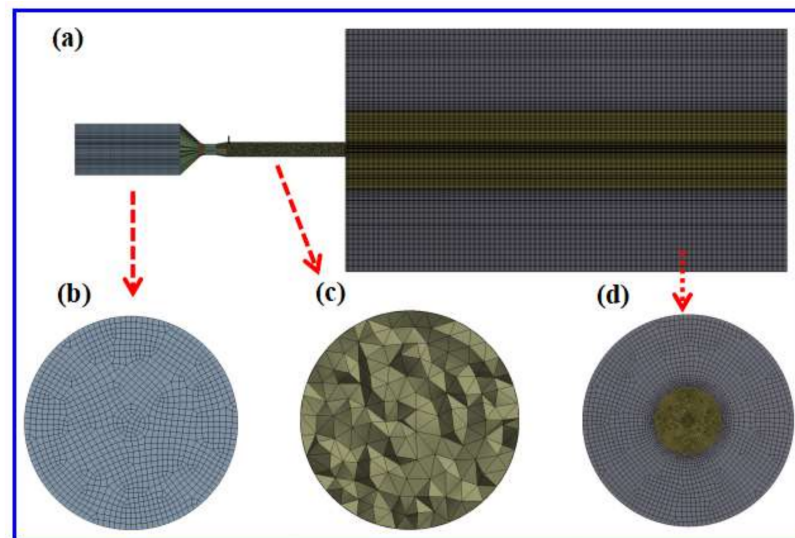
Figure 2. (**a**) Computational mesh of the model, (**b**) combustion chamber mesh, (**c**) barrel mesh, and (**d**) external region mesh.

Table 2. Powder properties of SAM1651 [29].

Powder Properties	Values
Density	7310 kg/m^3
Melting temperature	1394 K
Specific heat capacity	460 J/(kg K)
Thermal conductivity	22.5 W/(m K)
Latent heat of fusion	$3.25 \cdot 10^5$ J/kg

A realizable k–ε model is used, and within the Cartesian tensor, the governing equations of the 3D model are defined as follows [16,30]:

Mass conservation equation:

$$\frac{\partial \rho}{\partial t} + \frac{\partial}{\partial x_i}(\rho u_i) = 0 \tag{1}$$

Momentum conservation:

$$\frac{\partial}{\partial t}(\rho u_i) + \frac{\partial}{\partial x_j}(\rho u_i u_j) = -\frac{\partial p}{\partial x_i} + \frac{\partial}{\partial x_j}(\tau_{ij})_{eff} + \frac{\partial}{\partial x_j}\left(-\rho \overrightarrow{u'_i u'_j}\right) \tag{2}$$

Energy transport equation:

$$\frac{\partial}{\partial t}(\rho E) + \frac{\partial}{\partial x_i}(u_i(\rho E + p)) = \frac{\partial}{\partial x_j}\left(k_{eff}\frac{\partial T}{\partial x_j} + u_i(\tau_{ij})_{eff}\right) + S_h \tag{3}$$

The deviatoric stress tensor is

$$(\tau_{ij})_{eff} = \mu_{eff}\left(\frac{\partial u_j}{\partial x_i} + \frac{\partial u_i}{\partial x_j}\right) - \frac{2}{3}\mu_{eff}\frac{\partial u_i}{\partial x_i}\delta_{ij} \tag{4}$$

The effective thermal conductivity is

$$k_{eff} = k + \frac{c_p \mu_t}{\sigma_t} \tag{5}$$

Mass fraction conservation equation was added to the transport equations, and species transport model was customized to simulate the combustion reaction. The convection sources, diffusion sources, and reaction sources of the transport equation are described in [31]:

$$\frac{\partial}{\partial x_i}(\rho Y_\alpha u_i) = -\frac{\partial J_{\alpha,i}}{\partial x_i} + R_\alpha + S_\alpha, \ \alpha = 1, \ 2, \ ..., \ N-1 \tag{6}$$

In this study, the eddy dissipation model is used [32], which assumes that the combustion rate is decided by the blending rate of fuel and oxidants. The consumption rate of fuel is given by [33]:

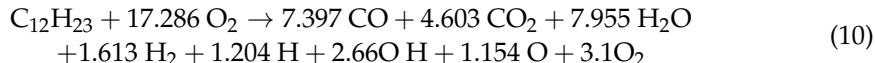$$R_F = -\frac{\rho\varepsilon}{k} A \min\left(mF, \frac{m_0}{s_0}, \ B\frac{m_p}{S_p}\right) \tag{7}$$

where

$$S_o \equiv \frac{n_o M_o}{n_F M_F} \tag{8}$$

$$S_P \equiv \frac{n_p M_o}{n_F M_F} \tag{9}$$

The empirical constants A and B are 4 and 0.5, respectively.

In practice, kerosene fuel is a mixture of alkanes with carbon content ranging from 9 to 17. Therefore, there is no precise chemical formula for kerosene. In the simulation, $C_{12}H_{23}$ is used as the representative average of the individual component of the kerosene. Because the combustion chamber's temperature exceeds 2300 K, H_2O and CO_2 break down into several lightweight mass substances, not solely to H_2 and CO flammable gases, however, additionally to O, H, OH, and other atomic gases [16]. The combustion dynamics is described by a global reaction [31] that accounts for intermediate and dissociation reactions.

$$C_{12}H_{23} + 17.286\,O_2 \rightarrow 7.397\,CO + 4.603\,CO_2 + 7.955\,H_2O$$
$$+1.613\,H_2 + 1.204\,H + 2.66O\,H + 1.154\,O + 3.1O_2 \tag{10}$$

In solving the Navier–Stokes equation, gases are treated as continuous phases, dispersed particle phases are solved by tracking large droplets, and there is no interaction between the particles. The trajectories of these discrete phases and the thermal transfer are calculated.

In Cartesian coordinates, the equations of particle motion in x direction can be written as a force balance, equating droplet inertia with forces acting on the particle; the basic particle equation is as follows.

$$\frac{du_p}{dt} = F_D\left(\mu - \mu_p\right) + F_x = \frac{18\mu}{\rho_p d_p^2}\frac{C_D Re}{24}\left(\mu - \mu_p + F_x\right) \tag{11}$$

A single-particle energy equation that ignores radiation heat transfer is shown below:

$$m_p c_p \frac{dT_p}{dt} = h_c A p\left(T_g - T_p\right) \tag{12}$$

The CFD commercial software (Fluent 19.0) is used, and the calculation is run on a GTS2-RIS208Q workstation. First, a 3D model for the JP5220 gun is established. Second, the boundary conditions, combustion reaction model, and gas flow model are established. To avoid simulation calculation divergence, all equations use the second-order upwind discretization method. Third, according to the convergence criterion to determine whether the calculation results converge; if convergence has been reached, then we end the calculation.

3. Results and Discussion

3.1. Flame Flow Characteristics

Figure 3 shows the simulation results of the flame flow characteristics (gas velocity, gas pressure, and gas temperature as well as the Mach number). The calculation shows that the flow characteristics of the flame change with the axial distance in the spraying process. The velocity, pressure, and temperature distribution have symmetrical distributions above and below the centerline of the gun body. As can be seen from Figure 3a, due to the large inlet oxygen flow rate, the gas behavior in the combustion chamber is streamlined along the symmetry axis. The overall gas velocity distribution in the combustion chamber is uniform but relatively low at 130 m/s. As the flame flows through the Laval nozzle, the velocity quickly exceeds 2000 m/s. Figure 3b illustrates the changes in the flame flow pressure during spraying, and the gas pressure is approximately 0.9 MPa in the combustion chamber. Due to the convergence of the spray nozzle, the pressure drops sharply to 0.18 MPa after passing through the nozzle and then exhibits overall stable distribution and slight local fluctuations. On the right side of the barrel outlet, the pressure profile alternates between light and dark conditions. The pressure value oscillations decrease and then stabilize at a fixed distribution of 0.1 MPa.
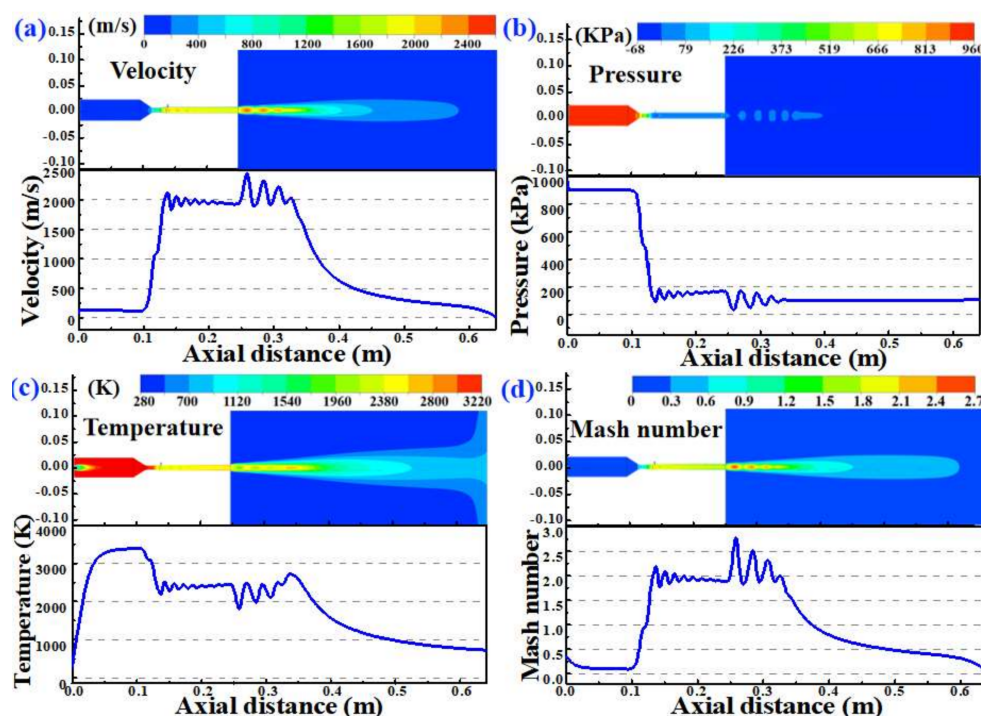

Figure 3. Contours of the flame flow and gas characteristics along the centerline for (**a**) gas velocity, (**b**) gas pressure, (**c**) gas temperature, and (**d**) Mach number.

As seen in Figure 3c, the initial temperature is relatively low because the kerosene and oxygen are not mixed sufficiently. With the combustion intensifies, the combustion chamber flame flow temperature peaks at 3400 K. When the flame flows through the spray nozzle, the temperature drops significantly and then fluctuates slightly toward a constant of 2400 K. The contour shows that when the flame flows into the cold air, the axial temperature continues to decrease after periodic fluctuations. Eventually, the temperature drops to 650 K at the substrate position. This whole process reflects the attenuation process of kerosene combustion energy. Figure 3d represents the changes in the Mach number, which are similar in trend to the flame flow velocity.

3.2. The Mass Fraction of Gas Components

In order to reveal the reaction mechanism of kerosene–oxygen combustion, the variation contours and curves of the mass fraction of various combustion components are shown in Figure 4. Red lines show the mass fraction of each component distributed along the centerline, with the horizontal and vertical axes in units of m. At the gun inlet, the mass fractions are only kerosene and oxygen. The temperature rises rapidly as the combustion reaction occurs. Concurrently, the temperature increase also promotes the diffusion of kerosene and oxygen, which intensifies the combustion reaction, and the mass fractions of the kerosene and oxygen decrease rapidly, whereas the mass fractions of the other combustion products increase rapidly [34]. The calculation results show that the concentration of kerosene flight into the combustion chamber is comparatively high in the axial direction. When mixture intensifies and burns completely, kerosene is consumed rapidly until its mass fraction decreases to zero in the combustion chamber. Simultaneously, oxygen acts as a flammable agent with relatively large inlet concentrations and oxygen declines rapidly in combustion chamber. In addition, oxygen increases in external region due to the presence of oxygen in the air. The concentrations of the combustion products H_2O, CO_2, and CO are relatively high, i.e., more than 0.2, and the concentrations of other gases are comparatively low.
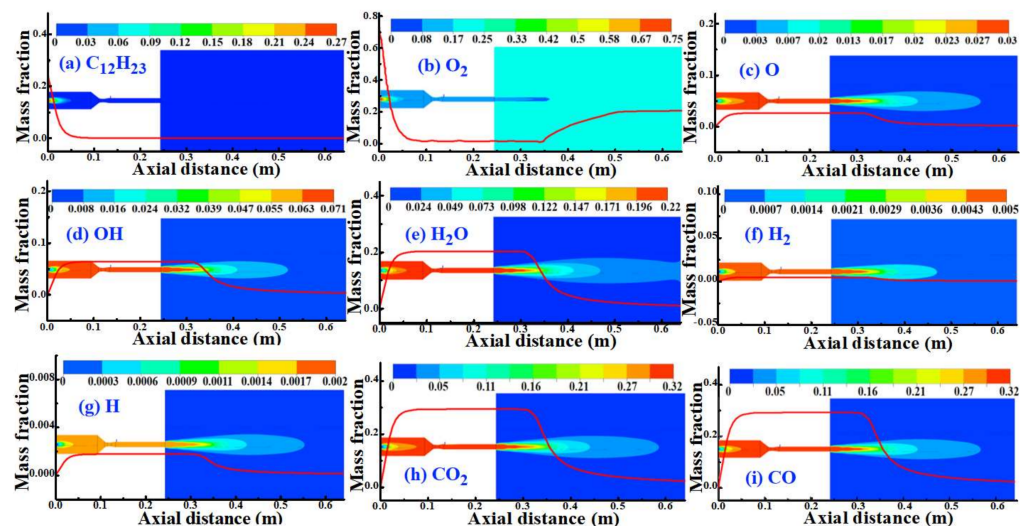

Figure 4. Contours and curves of the mass fraction of various components; (**a**) $C_{12}H_{23}$ (**b**) O_2 (**c**) O (**d**) OH € H_2O (**f**) H_2 (**g**) H (**h**) CO_2, and (**i**) CO.

3.3. Effect of the Oxygen/Fuel Ratio on Flame Flow

The O/F ratio is a pivotal variable for regulating the flame flow characteristics during the HVOF process [22,27]. According to the kerosene–oxygen combustion reaction formula (Equation (10)), the ideal conditions for full combustion of 1 L kerosene requires a mass ratio of oxygen 3.09 times that of kerosene. To further explore the influence of oxygen and kerosene on HVOF spraying, this study sets 11 comparative conditions to analyze the influence of different O/F ratios and the same O/F ratio but different total fuel oxygen amounts on the pressure, temperature, and velocity of the flame flow. The specific O/F ratio conditions are shown in Table 3 and Figure 5.

The characteristic curves for different O/F ratios are simulated and plotted, as shown in Figure 6. Through comparison, the pressure differences in the spray gun are mainly observed in the combustion chamber. The pressure in the platform region of the combustion chamber is compared, as shown in Figure 6d, and the pressure increases with the increasing O/F ratio. However, when the O/F ratio is 3.4, the pressure reaches the maximum and then decreases. Interestingly, the maximum pressure does not occur at the ideal O/F ratio of 3.09. At the barrel outlet, all curves exhibit low-amplitude fluctuations. Comparing

condition 4 with conditions 8–11, the changes in the pressure observed when adjusting the total amount of kerosene and oxygen under the condition of a fixed O/F ratio are analyzed. The combustion chamber pressure increases as the total fuel increases.

Table 3. Details of oxygen/fuel ratio conditions.

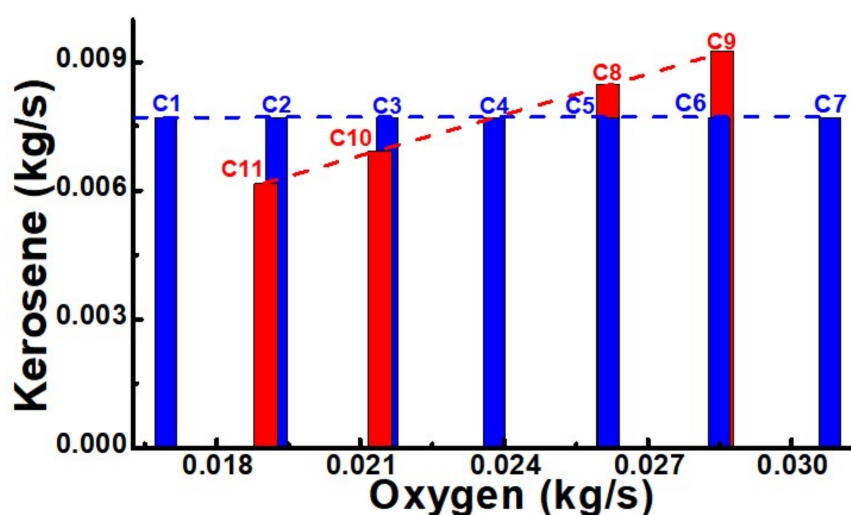| Condition	Kerosene (kg/s)	Oxygen (kg/s)	O/F Ratio
Condition 1	0.0077	0.01694	2.2
Condition 2	0.0077	0.01925	2.5
Condition 3	0.0077	0.02156	2.8
Condition 4	0.0077	0.02379	3.09
Condition 5	0.0077	0.02618	3.4
Condition 6	0.0077	0.02849	3.7
Condition 7	0.0077	0.0308	4
Condition 8	0.00847	0.02617	3.09
Condition 9	0.00924	0.02855	3.09
Condition 10	0.00693	0.02141	3.09
Condition 11	0.00616	0.01903	3.09

Figure 5. Details of oxygen/fuel ratio conditions.

According to the temperature analysis curves in Figure 6b,e, the O/F ratio has a certain influence on the heating rate of the combustion chamber. The higher the O/F ratio is, the higher is the slope of the curve in Figure 6b is. When the O/F ratio is fixed at 3.09, the slope of the temperature increase is the same. However, the maximum temperature does not monotonically increase with the increasing of O/F ratio, which is the same as in the case of pressure. The maximum temperature appears when the O/F is 3.4; then, the temperature decreases. The flame flow temperature does not increase significantly when the fuel mass increases by 10% or 20%, and the flame flow temperature does not decrease significantly when the fuel mass decreases by 10%. However, the temperature decreases significantly when the fuel mass is reduced by 20%, indicating that the total fuel quantity has no significant effect on the temperature within a certain fluctuation range. The final flame flow temperature decreases because of the effect of the cold air outside the spray gun on the flame flow. Due to the heat transfer between the air and the flame flow, the higher the temperature at the nozzle outlet, the faster the cooling rate. As shown in Figure 6c,f, the O/F ratio has an effect similar to that of the pressure and temperature on the velocity of the flame flow. As can be seen from the momentum equation, the higher the flame pressure, the faster the flame velocity. However, the variation trends of velocity and pressure are not the same. The maximum velocity appears when the O/F ratio is 3.7. Adjustments of the total fuel amount have a significant effects on speed with the fixed O/F ratio of 3.09, which changes in the same way as pressure.
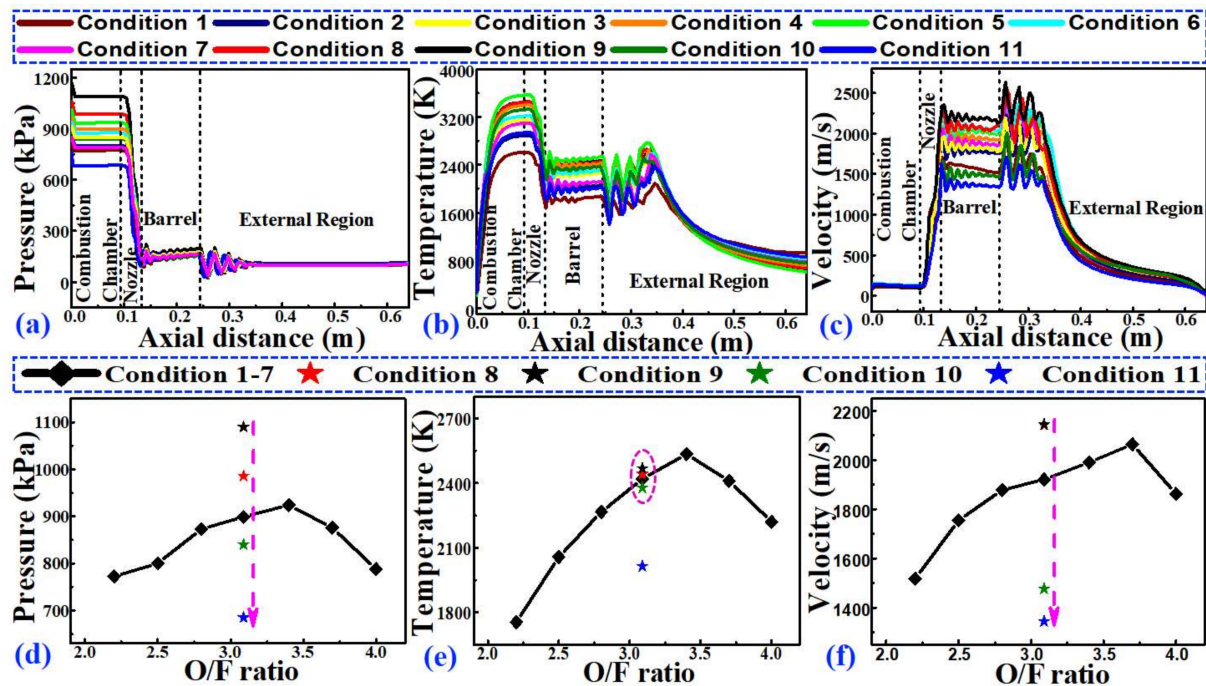
Figure 6. Predicted (**a**,**d**) gas pressure, (**b**,**e**) gas temperature, and (**c**,**f**) gas velocity curves with different O/F ratios.

At values higher than the ideal O/F ratio 3.09, an oxidizing environment forms, resulting in excessive oxidation of molten powder particles and an increase in the oxide content of the coating. If the ratio is less than 3.09, a large amount kerosene in the mixture will produce a flame with low temperature and poor oxygen content, and the number of unmelted particles and holes in the coating will increase. In fact, the ideal combustion conditions do not exist; to induce the full combustion of kerosene, usually, values higher than the ideal ratio are chosen for this spraying parameter. Combined with our work, it is intuitive that when the O/F quantitative relation is 3.4, the kerosene and oxygen can be totally combusted and the temperature and velocity of the flame flow are also optimal.

3.4. Effect of the Particle Size on Particle Behavior

Particle size is one of the most important factors affecting particle behavior. Particles of different sizes have different dynamic behaviors due to differences in their momentum. We selected six different particle sizes, fixed the O/F ratio at 3.4, and fixed the particle flow and nitrogen flow at 30 g/min and 10 m/s, respectively. The particles temperature and velocity curves with different sizes are simulated, as shown in Figure 7.

As can be seen from Figure 7a, small-sized particles are can be heated more than large particles; furthermore, their thermal inertia is smaller than that of large particles, so the temperature decreases faster. The liquid temperature T_l and solid temperature T_S of SAM1651 amorphous alloy are shown. The results show that 5–10 μm particles endure melting and solidifying throughout flight. The 20 and 30 μm particles remain melted; however, particles greater than 40 μm in size may not melt before they reach the substrate. With the increase in the particle size, the dynamic and thermal response of particles becomes slower than that of smaller particles, but the insulation capacity of large particles is stronger than that of smaller particles. Small particles are susceptible to heat but have a weaker ability to keep warm [24,35]. The melting behavior of the amorphous alloy powder is closely related to the amorphous phase content of the coating. The more fully melted the powder is, the more amorphous are the phases formed in the coating. When the particles hit the substrate in a molten or semimolten state, the splash thickness decreases, resulting in faster cooling and optimum corrosion resistance [36]. However, the amorphous phase content is low in the unmelted particles due to the presence of the crystal

phase. Figure 7b shows that the small particles are susceptible to gas flow due to higher heating rates. However, due to their relatively large resistance, the reduction is greater as the distance increases from the outlet of the spray gun. Although the speed of large particles increases slowly, they tend to maintain axial velocity given their greater inertia.
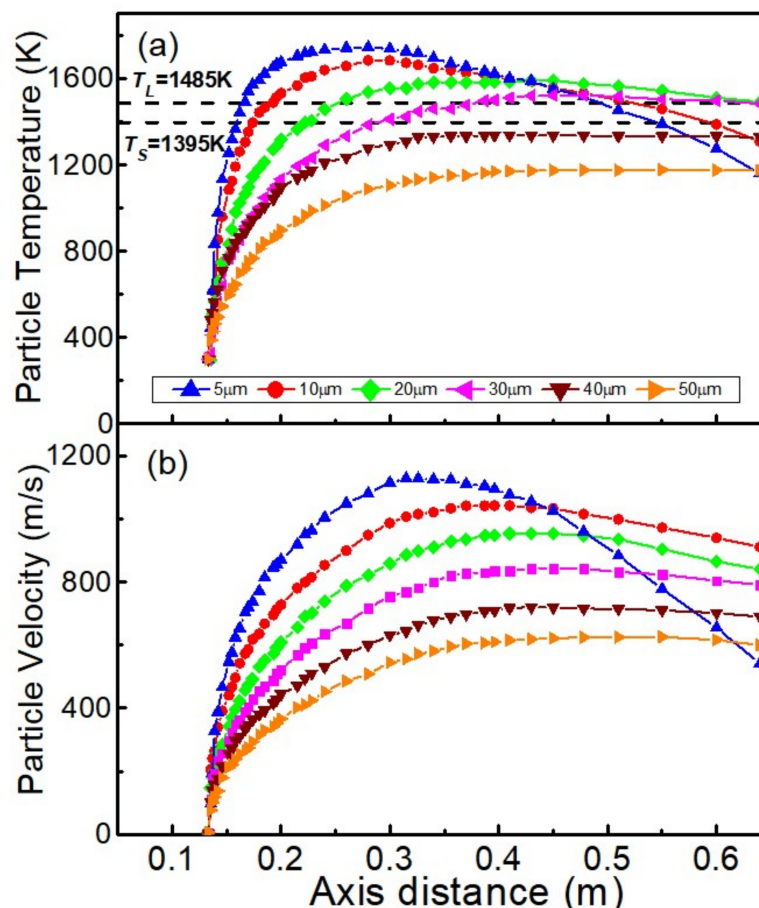

Figure 7. Effect of the particle size on the particle behavior for (**a**) particle temperature and (**b**) velocity.

To better analyze the effect of different particle sizes on coating properties, the particle trajectories under six conditions and the distribution of particles on X65 steel substrate are compared 0.04 s after the spraying process reaches the steady state. Figure 8 shows the particle flight behavior for various particle sizes with an injection rate of 10 m/s. As shown in Figure 8a, the small 5 μm particles move along the edge of the barrel. When the particles affect the substrate, they are concentrated in the upper half of the substrate and the local thickness of the coating is large. As the particle size increases, the radial motion distance of the particle increases. Large particles exhibit greater inertia than that of smaller; therefore, they maintain a radial motion and move a greater distance from the spray gun. Although 10 μm particles do not travel along the upper barrel, they are still mainly distributed in the upper half of the substrate. As shown in Figure 8c,d, the 20 and 30 μm particles move closer to the centerline of the external region and are evenly distributed on the substrate. Concurrently, the mass concentration of the coating with 30 μm particles is higher, indicating that the coating thickness and deposition efficiency are higher than those of the 20 μm particles. Figure 8f shows that when the particle size is large, the axial motion of the particle is close to the lower edge of the barrel and the particle distribution is concentrated in the lower part of the substrate, and a similar result was also observed in a past study [7].
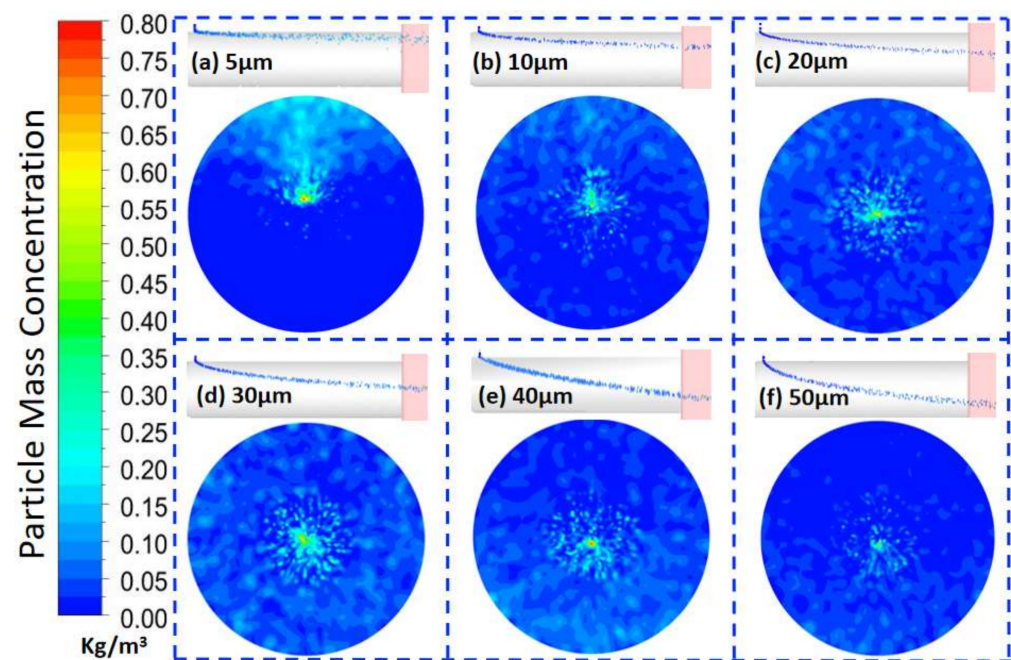
Figure 8. Effect of the particle size on particle trajectory and distribution.

According to the particle temperature and velocity curves, the particle size has an important influence in determining the particle temperature and velocity. In addition, according to the experiment, when the particle diameter is too small (less than 15 μm), the powder and nozzle exhibit a serious adhesion phenomenon, affecting the coating deposition rate. The degree of heating reduces greatly with particle diameters larger than 50 μm, which affects the deposition rate and surface quality of the coating. Compared with the small particles, when the particle size increases, the unmelted particles increase in number and the coating porosity increases. However, the amorphous alloy coating passive film prepared with large size powder particles is more stable than that of prepared with small particles [37]. The smaller the particle size, the larger is the surface area, and the higher the degree of oxidation is during spraying. As discussed above, the melting state is best when the particle size of the amorphous alloy powder is 20–30 μm and the prepared coating has a more uniform structure and excellent corrosion resistance.

3.5. Effect of Particle Shape on Particle Behavior

In this study, gas phase atomization is used to prepare an Fe-based amorphous alloy powder, a large number of nonspherical amorphous alloy particles inevitably exist. Previous studies have shown that the particle shape is related to particle motion resistance. With the increase in the particle sphericity, the drag decreases [38,39]. Figure 9 shows the temperature and velocity behavior of amorphous particles with different shapes when the particle size is 30 μm and the injection velocity is 10 m/s. As shown in Figure 9a, the particle temperature curves demonstrate that the temperatures of nonspherical powder particles are lower than those of spherical particles. Only when the sphericity is 1 or 0.9 does the particle temperature reach the molten or semimolten state. From Figure 9b, it can be seen that the nonspherical particles have a higher velocity. When the shape factor is reduced from 1 to 0.6, the nonspherical particles attain greater velocity and shorter times in the flame flow, which in turn brings their temperature down. Kamnis and Gu found similar results in particle spheres [40]. The flight behavior of the nonspherical WC–Co powder in an HVOF spray gun was simulated. Kamnis and Gu found that the nonspherical particles had a higher axial velocity and a lower temperature than spherical particles and were closer to the centerline of the torch. When the particle size decreases, the spherical degree has little effect on particle behavior.
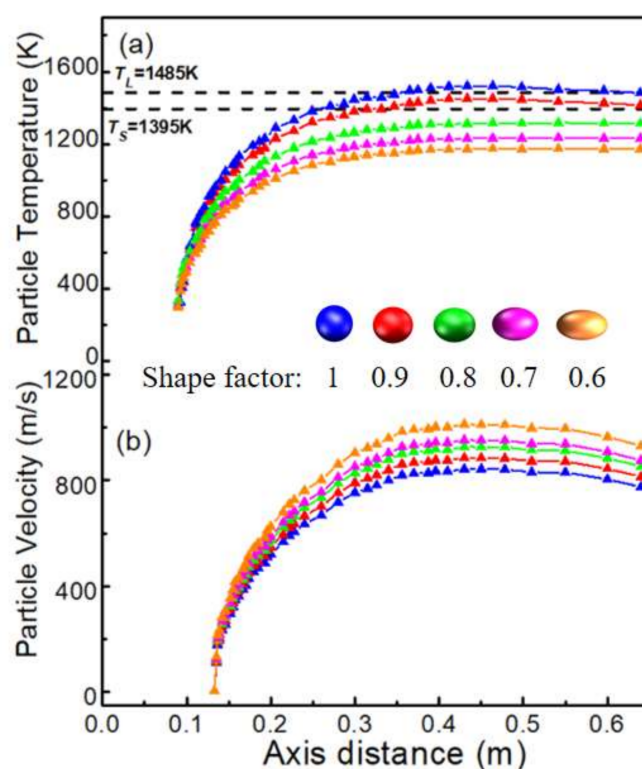
Figure 9. Effect of the particle shape on particle characteristics for (**a**) temperature and (**b**) velocity.

3.6. Effect of the Nitrogen Flow Rate and Particle Injection Rate on Particle Dynamics

The effect of the nitrogen injection rate and particle injection rate on amorphous particle dynamics has been studied in the literature [41–45]. In general, because nitrogen is inert and does not participate in combustion reactions, increasing the flow of nitrogen reduces its flow temperature and velocity [46]. The effect of different nitrogen flow and amorphous particle injection rates on HVOF-sprayed amorphous alloy coatings are compared and analyzed when the O/F ratio and particle size are fixed. In Figure 10a,b,d, it can be seen that when the nitrogen flow rate is 10 m/s, the particles move along the centerline of the spray gun and are evenly distributed on the substrate. When the nitrogen flow is 5 m/s, the particles move along the upper part of the gun and are concentrated in the upper part of the substrate. When the nitrogen flow rate is 20 m/s, the particles rebound after colliding with the inner wall of the spray barrel, changing the original trajectory and increasing the likelihood that the particles will adhere to the wall of the cylinder. At the same time, particle attachments lower the diameter of the spray gun barrel, further undermining the stability of the flame flow.

In addition, Figure 10b,c compare the fixed nitrogen flow at 10 m/s with different particle injection rates. The results show that the particle injection rate has no effect on the particle trajectory. However, the thickness of the coating (particle mass concentration) increases with the increasing particle injection rate. In HVOF spraying, the coating is deposited layer by layer. At the time the first layer formed, the temperature difference between the substrate and amorphous particles was large and the cooling rate of the amorphous alloy powder was the largest, approximately 10^6 K/s. In general, amorphous alloys display a lower heat conductivity [47–49], so the coating forms a temperature gradient along the depth of the coating [50,51]. The amorphous phase content of the coating decreases with the increase in the thickness.
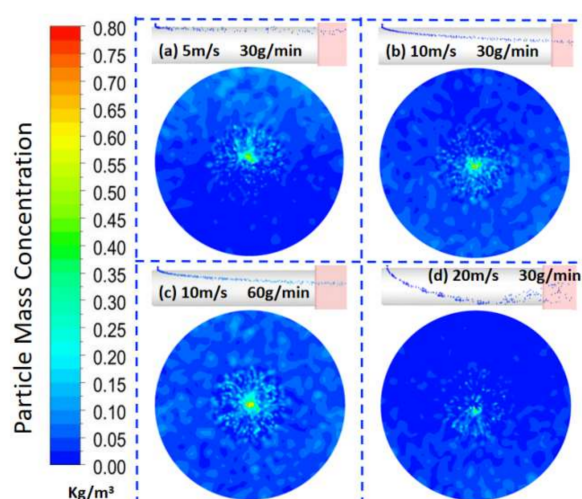
Figure 10. Effect of the nitrogen flow rate and particle injection rate on particle dynamics.

3.7. Effect of the Injection Angle of the Particle

We injected 30 μm particles at a nitrogen flow rate of 10 m/s. The trajectories of particles with injection angles of −45°, −30°, 0°, 30°, and 45° are simulated, as shown in Figure 11. As can be seen from Figure 11a, when the injection angle is in the opposite direction to the flame flow, the particle temperature is higher than that of the vertical injection particles. Because particles encounter high-temperature flame flow, more heat is generated. In contrast, when particles are shot in the direction of the flame, the temperature of the particles is lower than the temperature of the vertical injection particles. In addition, except for the particles at the −45° injection angle, the temperature differences between the other four angles are not large and the particles can melt well. Figure 11b shows the particle velocity during flight. The particles have the maximum velocity when the injection angle is 0°, and the velocity at the other four angles decreases slightly. Similar to the temperature behavior, the particles at −45° have the lowest velocity. Referring to the particle movement trajectories in Figure 11c, it is found that when the injection angle is −45°, the particles move along the upper gun wall and deviate from the flame flow's centerline. The best injection angle to obtain high temperature and low velocity is 45°. The precise selection of an injection angle not only ensures that the particles obtain reasonable temperature and velocity but also helps control the particles deposition position.
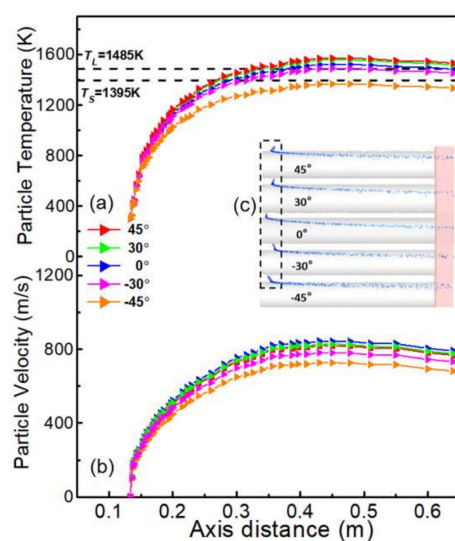

Figure 11. Effect of the particle injection angle on the particle behavior for (**a**) particle temperature, (**b**) velocity, and (**c**) trajectories.

4. Conclusions

A 3D CFD model is established using the Fluent software to study flame flow and amorphous alloy particle behavior in the HVOF spray process. The gas pressure, temperature, velocity, gas component, and amorphous alloy particle morphology and deposition patterns were examined in the HVOF spray process. Based on the results of numerical simulation, the following three conclusions can be obtained.

1. During the HVOF spraying process, the temperature, velocity, and pressure of flame flow appear the maximum value near O/F ratio of 3.4. When the O/F ratio is fixed, the flame flow pressure and velocity increases monotonically with the increases in the total fuel flow rate, but the total fuel flow rate has no significant effect on flame flow temperature.
2. Particle size and shape have an important influence on particle melting state and movement behavior. When the particle size of the amorphous alloy powder is 20–30 μm, the particles are evenly distributed on the substrate with high mass concentration. When the particle sphericity is 1 or 0.9, the particle reaches the molten or semimolten state. The prepared coating has a more uniform structure and low porosity.
3. Nitrogen flow rate, particle injection rate, and angle have a great influence on HVOF spraying amorphous alloy coating. When the nitrogen flow rate is 10 m/s, the particles move along the centerline of the spray gun and are evenly distributed on the substrate. The increase in the particle injection rate can increase the coating thickness (particle mass concentration) but has no effect on particle trajectory. The best incident angle is 45°, which not only ensures that the particles obtain reasonable temperature and velocity but also helps control the particle deposition.

This study is helpful to understand the process of preparing Fe-based amorphous alloy coatings by HVOF spraying, deepen the understanding of flame flow and particle behavior, and provide theoretical guidance for the improvement of HVOF spraying equipment and selection of manufacturing parameters.

Author Contributions: Conceptualization, X.L. and P.L. (Pengfei Liu); Data curation, P.L. (Pengfei Liu); Formal analysis, X.L.; Funding acquisition, J.Y. and Y.Y.; Investigation, X.L. and H.L.; Project administration, X.L. and Y.Y.; Resources, J.Y.; Software, X.L. and R.S.; Validation, H.L.; Writing—original draft, X.L., L.W. and P.L. (Pengfei Li); Writing—review & editing, X.L. and P.L. (Pengfei Li). All authors have read and agreed to the published version of the manuscript.

Institutional Review Board Statement: Not applicable.

Informed Consent Statement: Not applicable.

Data Availability Statement: Data sharing is not applicable to this article.

Conflicts of Interest: There are no conflicts of interest to declare.

Nomenclature

C_p	specific heat, J/(kg·K)
E	enthalpy value
K_{eff}	kinetic energy in turbulent and nonturbulent flow
u_{eff}	the addition of nonturbulent viscosity
k	thermal conductivity
R_a	net productivity
S_a	productivity
S_h	reaction source energy

x_i	coordinate in the i direction
J_a	mass diffusion flux
δ	Kronecker delta
σ_t	turbulent Prandtl number
T	temperature
T_g	glass transition temperature
T_l	liquid temperature
T_s	solid temperature
τ	deviatoric stress tensor
T	turbulent environment
p	pressure, Pa
ρ	density, kg/m^3
u_i	velocity in the i direction
μ_t	turbulent viscosity
Y_a	mass fraction of product a

References

1. Hou, B.; Li, X.; Ma, X.; Du, C.; Zhang, D.; Zheng, M.; Ma, F. The cost of corrosion in China. *J. NPJ Mater. Degrad.* **2017**, *1*, 4. [CrossRef]
2. Shen, J.; Chen, Q.; Sun, J.; Fan, H.; Wang, G. Exceptionally high glass-forming ability of an FeCoCrMoCBY alloy. *J. Appl. Phys. Lett.* **2005**, *86*, 279. [CrossRef]
3. Xu, D.; Duan, G.; Johnson, W.L. Unusual Glass-Forming Ability of Bulk Amorphous Alloys Based on Ordinary Metal Copper. *J. Phys. Rev. Lett.* **2004**, *92*, 245504. [CrossRef] [PubMed]
4. Amjad, I.; Sumera, S.; Moazam, M.; Muhammad, Y. Comparative analysis on the structure and properties of iron-based amorphous coating sprayed with the thermal spraying techniques. *Coatings* **2020**, *10*, 1003.
5. Wei, H.W. Roles of minor additions in formation and properties of bulk metallic glasses. *J. Prog. Mater. Sci.* **2007**, *52*, 540–596.
6. Ramya, M.; Karthika, M.; Selvakumar, R.; Raj, B.; Ravi, K.R. A facile and efficient single step ball milling process for synthesis of partially amorphous Mg-Zn-Ca alloy powders for dye degradation. *J. Alloy. Compd.* **2017**, *696*, 185–192. [CrossRef]
7. Lan, S.; Ren, Y.; Wei, X.; Wang, B.; Gilbert, E.P.; Shibayama, T. Hidden amorphous phase and reentrant supercooled liquid in Pd-Ni-P metallic glasses. *Nat. Commun.* **2017**, *8*, 14679. [CrossRef]
8. Li, X.; Roberts, M.; O'Keeffe, S.; Sercombe, T. Selective laser melting of Zr-based bulk metallic glasses: Processing, microstructure and mechanical properties. *Mater. Des.* **2016**, *112*, 217–226. [CrossRef]
9. Tului, M.; Bartuli, C.; Bezzon, A.; Marino, A.L.; Marra, F.; Matera, S.; Pulci, G. Amorphous steel coatings deposited by cold-gas spraying. *Metals* **2019**, *9*, 678. [CrossRef]
10. Lin, T.-J.; Sheu, H.-H.; Lee, C.-Y.; Lee, H.-B. The study of mechanical properties and corrosion behavior of the Fe-based amorphous alloy coatings using high velocity oxygen fuel spraying. *J. Alloy. Compd.* **2021**, *867*, 159132. [CrossRef]
11. Jadidi, M.; Moghtadernejad, S.; Dolatabadi, A. A comprehensive review on fluid dynamics and transport of suspension/liquid droplets and particles in High-velocity oxygen fuel (HVOF) thermal spray. *Coatings* **2015**, *5*, 576–645. [CrossRef]
12. Zhu, Y.Y.; Li, Z.G.; Li, R.F.; Li, M.; Feng, K.; Wu, Y.X.; Kato, H. High power diode laser cladding of Fe-Co-B-Si-C-Nb amorphous coating: Layered microstructure and properties. *J. Surf. Coat. Technol.* **2013**, *235*, 699–705. [CrossRef]
13. Li, G.; Gan, Y.; Liu, C.; Shi, Y.; Zhao, Y.; Kou, S. Corrosion And Wear Resistance of Fe-Based Amorphous Coatings. *Coatings* **2020**, *10*, 73. [CrossRef]
14. Zhou, Z.; Han, F.X.; Yao, H.H.; Li, Y.Z.; Yang, Y.G.; Guo, X.Y.; Wang, L. Novel Fe-Based Amorphous composite coating with a unique interfacial layer improving thermal barrier application. *J. ACS Appl. Mater. Interfaces* **2021**, *13*, 23057–23066. [CrossRef] [PubMed]
15. Yoon, S.; Lee, C.; Choi, H.; Jo, H. Kinetic spraying deposition behavior of bulk amorphous NiTiZrSiSn feedstock. *J. Mater. Sci. Eng. A* **2005**, *415*, 45–52. [CrossRef]
16. Kamnis, S.; Gu, S. Numerical modelling of propane combustion in a high velocity oxygen–fuel thermal spray gun. *Chem. Eng. Process.* **2006**, *45*, 246–253. [CrossRef]
17. Li, M.; Christofides, P.D. Modelling and control of high-velocity oxygen-fuel (HVOF) thermal spray: A tutorial review. *J. Therm. Spray Technol.* **2009**, *18*, 753–768. [CrossRef]
18. Oksa, M.; Turunen, E.; Suhonen, T.; Varis, T.; Hannula, S.-P. Optimization and characterization of high velocity oxy-fuel sprayed coatings: Techniques, Materials, and applications. *J. Therm. Spray Coat.* **2011**, *1*, 17–52. [CrossRef]
19. Li, M.; Christofides, P.D. Modelling and analysis of HVOF thermal spray process accounting for powder size distribution. *Chem. Eng. Sci.* **2003**, *58*, 849–857. [CrossRef]
20. Tabbara, H.; Gu, S. Computational Simulation of Liquid-Fuelled HVOF Thermal Spraying. *Surf. Coat. Technol.* **2009**, *204*, 676–684. [CrossRef]
21. Oberkampf, W.L.; Talpallikar, M. Analysis of High-Velocity Oxygen-Fuel (HVOF) Thermal Spray Torch Part 1: Numerical Formulation. *J. Therm. Spray Technol.* **1996**, *5*, 53–68. [CrossRef]

22. Gu, S.; Eastwick, C.N.; Sirnmons, K.A.; McCartney, D.G. Computational Fluid Dynamic Modeling of Gas Flow Characteristics in a High-Velocity Oxy-Fuel Thermal Spray System. *J. Therm. Spray Technol.* **2001**, *10*, 461–469.

23. Sakaki, K.; Shimizu, Y. Effect of the Increase in the Entrance Convergent Section Length of the Gun Nozzle on the High-Velocity Oxygen Fuel and Cold Spray Process. *J. Therm. Spray Technol.* **2001**, *10*, 487–496. [CrossRef]

24. Yang, X.; Eidelman, S. Numerical Analysis of a High-Velocity OxygenFuel Thermal Spray System. *J. Therm. Spray Technol.* **1996**, *5*, 175–184. [CrossRef]

25. Dongmo, E.; Wenzelburger, M.; Gadow, R. Analysis and optimization of the HVOF process by combined experimental and numerical approaches. *Surf. Coat. Technol.* **2008**, *202*, 4470–4478. [CrossRef]

26. Liu, S.L.; Zheng, X.P.; Geng, G.Q. Influence of nano-WC-12Co powder addition in WC-10Co-4Cr AC-HVAF sprayed coatings on wear and erosion behavior. *Wear* **2010**, *269*, 362–367. [CrossRef]

27. Li, M.; Shi, D.; Christofides, P.D. Diamond Jet Hybrid HVOF Thermal Spray: Gas-Phase and Particle Behavior Modeling and Feedback Control Design. *Ind. Eng. Chem. Res.* **2004**, *43*, 3632–3652. [CrossRef]

28. Jadidi, M.; Yeganeh, A.Z.; Dolatabadi, A. Numerical Study of Suspension HVOF Spray and Particle Behavior Near Flat and Cylindrical Substrates. *J. Therm. Spray Technol.* **2018**, *27*, 59–72. [CrossRef]

29. Ajdelsztajn, L.; Dannenberg, J.; Lopez, J.; Yang, N.; Farmer, J.; Lavernia, E.J. High-velocity oxygen fuel thermal spray of Fe-based amorphous alloy: A numerical and experimental study. *Metall. Mater. Trans. A* **2009**, *40*, 2231–2240. [CrossRef]

30. Khan, M.N.; Shamim, T. Investigation of a dual-stage high velocity oxygen fuel thermal spray system. *Appl. Energy* **2014**, *130*, 853–862. [CrossRef]

31. Pan, J.; Hu, S.; Yang, L.; Ding, K.; Ma, B. Numerical analysis of flame and particle behavior in an HVOF thermal spray process. *Mater. Des.* **2016**, *96*, 370–376. [CrossRef]

32. Magnussen, B.F.; Hjertager, B.H.J.S.O.C. On Mathematical Modeling of Turbulent Combustion with Special Emphasis on Soot Formation and Combustion. *Symp. Int. Combust. Proc.* **1977**, *16*, 719–729. [CrossRef]

33. Emami, H.; Mahmoudi, Y. Effects of Combustion Model and Chemical Kinetics in Numerical Modeling of Hydrogen-Fueled Dual-Stage HVOF System. *J. Therm. Spray Technol.* **2019**, *28*, 333–345. [CrossRef]

34. Li, C.; Gao, X.; Zhang, D.; Gao, H.; Han, X.; Zhang, B. Numerical Investigation on the Flame Characteristics and Particle Behaviors in a HVOF Spray Process Using Kerosene as Fuel. *J. Therm. Spray Technol.* **2021**, *30*, 725–738. [CrossRef]

35. Pawlowski, L. *The Science and Engineering of Thermal Spray Coating*; John Wiley & Sons Ltd.: New York City, NY, USA, 2008; Volume 2.

36. Planche, M.P.; Liao, H.; Normand, B.; Coddet, C. Relationships between NiCrBSi particle characteristics and corresponding coating properties using diferent thermal spraying processes. *Surf. Coat. Technol.* **2005**, *200*, 2465. [CrossRef]

37. Farmer, J.C.; Haslam, J.J.; Day, S.D.; Lian, T.; Saw, C.K.; Hailey, P.D.; Aprigliano, L.F. Corrosion resistance of thermally sprayed high-boron iron-based amorphous-metal coatings: $Fe_{49.7}Cr_{17.7}Mn_{1.9}Mo_{7.4}W_{1.6}B_{15.2}C_{3.8}Si_{2.4}$. *J. Mater. Res.* **2007**, *22*, 2297. [CrossRef]

38. Cheng, D.; Xu, Q.; Trapaga, G.; Lavernia, E.J. The effect of particle size and morphology on the in-flflight behaviour of particles during high-velocity oxyfuel thermal spraying. *Metall. Mater. Trans. B* **2001**, *32*, 525–535. [CrossRef]

39. Ganser, G. A rotational approach to drag prediction of spherical and nonspherical particles. *Powder Technol.* **1993**, *77*, 143–152. [CrossRef]

40. Gu, S.; Kamnis, S. Numerical modelling of in-flight particle dynamics of non-spherical powder. *Surf. Coat. Technol.* **2009**, *203*, 3485–3490. [CrossRef]

41. Gu, S.; McCartney, D.G.; Eastwick, C.N.; Simmons, K. Numerical modelling of in-flight characteristics of inconel 625 particles during High-Velocity Oxy-Fuel thermal spraying of nanocrystalline materials: An overview. *Model. Simul. Mater. Sci. Eng.* **2002**, *11*, 1.

42. Li, M.; Christofides, P.D. Multi-scale modeling and analysis of an industrial HVOF thermal spray process. *Chem. Eng. Sci.* **2005**, *60*, 3649–3669. [CrossRef]

43. Hossainpour, S.; Binesh, A.R. A CFD study of sensitive parameter effects on the combustion in a High Velocity Oxygen Fuel thermal spray gun. *Proc. World Acad. Sci. Eng. Technol.* **2018**, *31*, 213–220.

44. Kamali, R.; Binesh, A.R. The importance of sensitive parameters effect on the combustion in a High Velocity Oxygen-Fuel spray system. *Int. Commun. Heat Mass Transf.* **2009**, *36*, 978–983. [CrossRef]

45. Chang, C.H.; Moore, R.L. Numerical simulation of gas and particle flow in a high velocity oxygen fuel (HVOF) torch. *J. Therm. Spray Technol.* **1995**, *4*, 358–366. [CrossRef]

46. Li, M.; Christofides, P.D. Computational study of particle in-flight behaviour in the HVOF thermal spray process. *Chem. Eng. Sci.* **2006**, *61*, 6540–6552. [CrossRef]

47. Shin, D.I.; Gitzhofer, F.; Moreau, C. Properties of induction plasma sprayed iron based nanostructured alloy coatings for metal based thermal barrier coatings. *J. Therm. Spray Technol.* **2007**, *16*, 118. [CrossRef]

48. Lee, K.; Euh, K.; Nam, D.H.; Lee, S.; Kim, N.J. Wear resistance and thermal conductivity for zr-base amorphous alloy/metal surface composites fabricated by high-energy electron beam irradiation. *Mater. Sci. Eng. A* **2007**, *449*, 937. [CrossRef]

49. Kim, J.; Lee, C.; Choi, H.; Jo, H.; Kim, H. Ni-Ti-Zr-Si-Sn bulk metallic glass particle deposition and coating formation vacuum plasma spraying. *Mater. Sci. Eng. A* **2007**, *449*, 858. [CrossRef]

50. Vardelle, A.; Moreau, C.; Fauchais, P. The dynamics of deposit formation in thermal-spray processes. *MRS Bull.* **2000**, *25*, 32. [CrossRef]
51. Sampath, S.; Herman, H. Rapid solidification and microstructure development during plasma spray deposition. *J. Therm. Spary. Technol.* **1996**, *5*, 445–456. [CrossRef]